POAC'13
Espoo, Finland

Proceedings of the 22nd International Conference on
Port and Ocean Engineering under Arctic Conditions
June 9-13, 2013
Espoo, Finland

ICE OBJECTS TRACKED FROM COASTAL RADAR IMAGE SEQUENCES AS VIRTUAL ICE BUOYS

Juha Karvonen [1], Istvan Heiler [1], Jari Haapala [1], Jonni Lehtiranta [1]
[1]Finnish Meteorological Institute (FMI), Helsinki, FINLAND

ABSTRACT

FMI has deployed image capturing devices into Finnish coastal radars. The captured Plan Position Indicator (PPI) radar images are transmitted to Finnish Meteorological Institute (FMI) via a GSM modem connection. We have also developed an ice object tracking algorithm, which first locates the traceable objects and then tracks them until the object tracking becomes unreliable. The reliability of the tracking is measured by a quality measure, and the object is lost when the quality value for the object falls below a given threshold value. The objects are initially located based on the local statistics of the first radar image of the image sequence. The tracking algorithm is based on a two-resolution combination of cross-correlation and phase correlation between two successive radar images. The objects tracked through a time series of radar images can be used as virtual ice buoys, giving information of the fine scale ice motion. We have studied some radar image sequences from two Baltic Sea coastal radars. The temporal sampling used in our experiments was 10 minutes. For these image sequences we have for example computed the virtual buoy mean velocities and strains. These computed results are also compared to the ice compression given by the operational HELMI (HELsinki Multi-category Ice model) ice model to resolve how these virtual buoy measures are related to the modelled ice compression.

1. INTRODUCTION

Ice drifter buoys are used to define the ice drift and the dynamic ice parameters, e.g. convergence, divergence, shear, ice compression. Even though ice drifters with GPS tracking are not very expensive, multiple buoys are required to estimate ice parameters related to ice dynamics with a reasonable accuracy, and this makes the total cost relatively high. FMI is operationally acquiring and storing data from some coastal radars in the Baltic Sea. In this study we have studied the possibility to use the ice objects recognized and tracked in the radar images as virtual ice buoys or drifters. The tracking algorithm was presented in (Karvonen, 2012) and it seems to work relatively reliably for the studied test cases. In this study we have performed ice tracking for some time periods during three winters (2010-2011, 2011-2012. 2012-2013). The cases in this study were selected such that the ice in the vicinity of the coastal radars is in motion. We also have computed ice strains for these cases, and qualitatively compared the results with the ice compression forecasts based on the HELMI ice model (Haapala 2000, Haapala et al., 2005).

2. RADAR IMAGE CAPTURING AND PREPROCESSING

The radar image capturing unit (radar video server) used by FMI has been developed by a Finnish company Image Soft Ltd. The radar video server has a 20 MHz sampling rate. It is

based on PC technology and forms PPI (Plan Position Indicator) images from the radar signal, the triggering pulse and the antenna pulse. PPI is the most common type of radar display. The radar antenna is represented at the center of the display, so the distance from it and height above ground can be drawn as concentric circles. The received radar signal contains information on the echo intensities and distances. Triggering and antenna pulses indicate when and in which direction the radar signal was sent. Azimuth Change Pulse (ACP) is a pulse set between a fixed angle in radar rotation. Typically there are 2^n pulses per 360 degrees. The Azimuth Reset Pulse (ARP) is a reference pulse set at a reference point. The radar angle is derived by counting the number of ACP pulses since the most recent ARP pulse. The images are constructed based on these pulses and on the recorded echoes with a known time difference.

For the two coastal radars, currently used by FMI, the total area imaged is 40 km by 40 km, and the image size is 1200x1200 pixels, resulting to a nominal resolution of about 33 m. Naturally the true resolution depends on the radar parameters, and in the far range the resolution is restricted by the angular (or bearing) resolution. The image origin, i.e. location of the radar is shifted such that the origin of our radar images is located at (30000m, 20000m) from the upper left corner of the images, i.e. the origin has been shifted to the east by 10 km. This was performed due to the fact that the two coastal radars are located in the eastern side of the Gulf of Bothnia, and after this shift we are able to see more sea area, which is our main interest, in the images. The Tankar coastal radar images are additionally rotated clockwise by 50 degrees, due to the shape of the coast at the location. After this rotation the Tankar radar images cover less land area, and the ship lead to the Kokkola harbor is better covered. A temporal median filtering is applied to the image data, using 9 first images for each whole minute (e.g. corresponding to nine seconds if the radar rotates 60 rounds per minute). This filtering reduces the radar imaging noise and also effectively filters some other undesired random effects (radar artifacts). In our experiments we use a ten minute time interval between each image pair of an image time series, i.e. we use temporally down-sampled data.

3. ICE TRACKING ALGORITHM

In the first image of an image sequence (time series), we must define the initial objects to trace and their locations. The traceable ice objects are selected based on local image statistics described by the local maxima of the local energy function E:

$$E(r,c) = \sigma(r,c,R)\, N_c(r,c,R)\, N_e(r,c,R) \quad (1)$$

In the equation $\sigma(r,c,R)$ is the local image pixel value standard deviation computed within the given radius R from the image location described by the row and column coordinates (r,c), $N_c(r,c)$ and $N_e(r,c)$ are the numbers of corner and edge points around (r,c), within the radius R from (r,c), respectively. We use a product form, because for a traceable object we want all the three terms to have a high value. The corner points are here computed using two algorithms, and all the points produced by either of the algorithms are included as edges. The first algorithm is the Harris corner detector (Harris & Stephens, 1988), and the other is based on local binary patterns (LBP) (Ojala et al., 1996).

The edges are located by the same algorithms as the corners, a corner pixel is actually just a special case of a detected edge pixel. After detecting the edges, we remove small edge segments, i.e. edge segments with a size smaller than a given number of connected edge

pixels. This filtering reduces the amount of edges produced by imaging noise. This procedure is described in detail in (Karvonen, 2012).

The tracking is performed for each pair of successive radar images of a radar image sequence, which here is a radar image time series with a constant temporal sampling rate of ten minutes. The object locations in the first image of the image pair are known (either based on the the initial object detection from the first image of an image sequence, or as a result of the tracking for later images). The algorithm is based on a combination of phase- and cross-correlations between the two image windows around the centres of the objects.

The phase- and cross-correlations are computed between two image windows sampled from two successive radar images in an image sequence. The correlations are also computed in two resolutions for each object, and the candidates for new location are located by finding the local combined correlation maxima. First, candidates for the motion are defined in a coarse resolution, and then the final motion estimate is defined in a fine scale. The tracking algorithm is described in detail in (Karvonen, 2012).

The tracking is performed for each virtual buoy, until a quality measure, describing the reliability of the tracking, becomes lower than a given threshold, for more details see (Karvonen, 2012). In the case the virtual buoys are continuously moving further from the coastal radar, at some point they are lost by the algorithm, after the quality value, due to the radar response fading in the far radar range, becomes too low for reliable tracking.

4. TRACKING RESULTS

We have studied the tracking for a few cases during winters 2010-2011, 2011-2012, and 2012-2013. The cases are from both Tankar (location 22.84E, 63.95N) and Marjaniemi (24.57E, 65.04N) coastal radars. The sampling rate of 10 minutes has proved to be sufficient for sea ice tracking. We show some tracking results (virtual buoy trajectories) in Fig. 1. These three examples are for the Tankar coastal radar area. We can see that the ice is drifting away from the coastal radar and fast ice near the coast in the 2011 and 2012 cases, and towards the fast ice in the 2013 case. The coastal radar location is shown as a brown square in the figures, different virtual buoy trajectories are shown in different colours.

For the 2011 case the ice drift relative to the fast ice is relatively uniform and many virtual buoys could be tracked through the period of about 14 hours, for 2012 case the tracking period was 24 hours, and only three moving buoys (in addition to the static buoys over the fast ice) could be tracked throughout the test period. It seems that when the ice is moving, 24 hours is a the maximum tracking period, and at least after this some more virtual buoys close to the coastal radar should be added to keep ice tracking continuous.

To study the general nature of the ice drift in each case, we computed the 10 minute mean ice velocities for the virtual buoys. Because in each case studied here the drift for the virtual drifting buoys was relatively uniform, we here demonstrate the behaviour by showing the velocities of one drifting buoy for each case. The velocities of the other drifting buoys in each case were also rather similar, naturally some small deviations existed, but we can consider these velocities presented for single virtual buoys characteristic for the ice drift during the test periods. The velocities for the selected buoys representing each case are shown in Fig. 2.

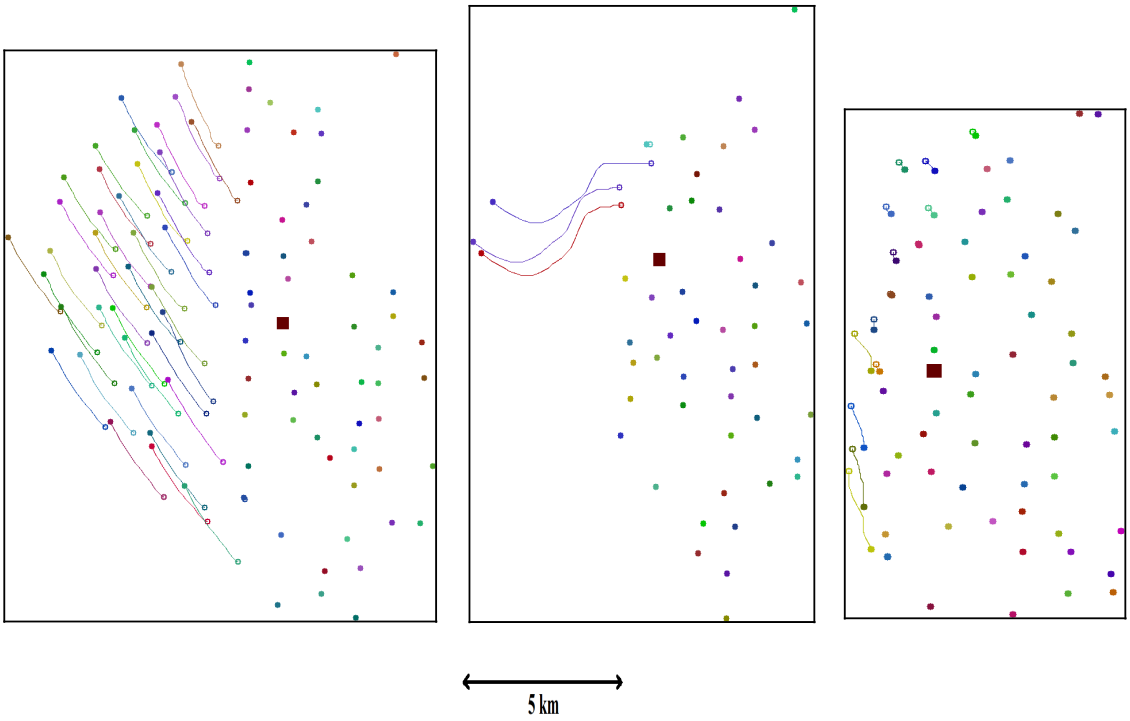

Figure 1. Tracked virtual buoys near Tankar coastal radar during the periods Feb 25, 2011 03:00-17:00 UTC (left); Feb 8, 2012 00:00-24:00 UTC (middle); and Jan 20, 2013 06:00-09.00 UTC (right). The starting points of the virtual buoys are indicated by an open circle and the ending points by a closed circle. The scale is indicated under the figures. The upward direction (y-axis) is 50 degrees.

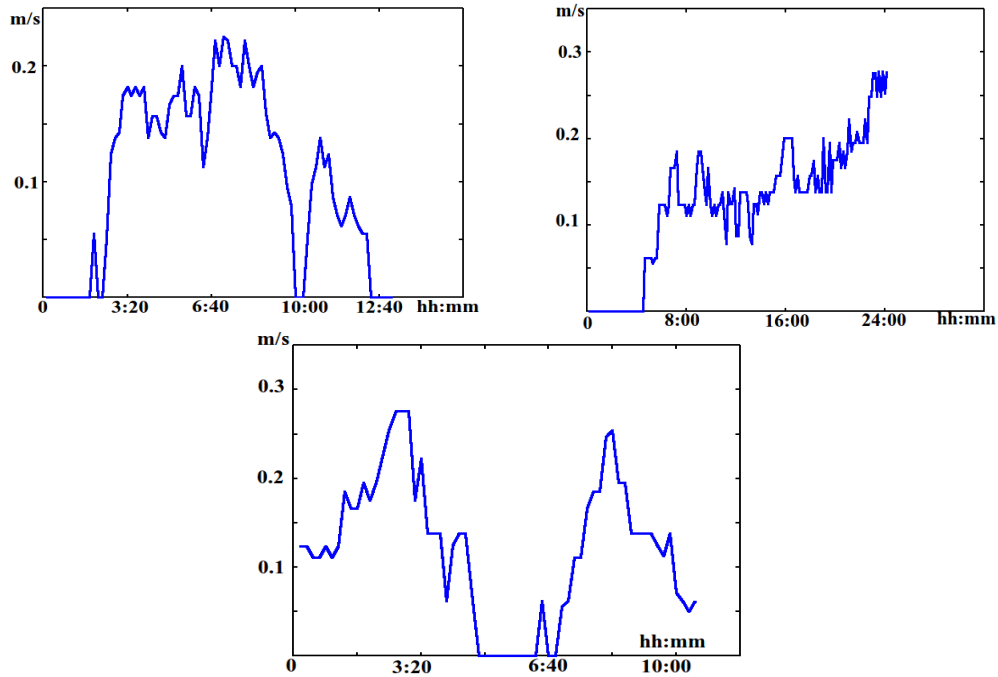

Figure 2. Velocities of characteristic drifting virtual buoys during the three test periods. Feb 25, 2011 (top left), Feb 8, 2012 (top right), and Jan 20, 2013 (bottom). The values on x-axis are times from the beginning of the period (hh:mm).

5. STRAIN COMPUTATION

Strain is a geometrical measure of deformation representing the relative displacement between particles in a material body, i.e. a measure of how much a given displacement locally differs from a rigid-body displacement. Sea-ice motion field can be decomposed into mean sea-ice motion, differential sea-ice motion and on rotational motion. Differential sea-ice motion can further be decomposed into divergent, convergent and shear motion. Sea-ice deformations (rafting, ridging and lead openings) are results of the differential ice motions, which in turn depend on the material properties of the sea-ice. The strain tensor can be defined in a matrix format:

$$\varepsilon_{ij} = \begin{pmatrix} \varepsilon_{xx} & \varepsilon_{xy} \\ \varepsilon_{yx} & \varepsilon_{yy} \end{pmatrix}, \tag{2}$$

where

$$\begin{aligned} \varepsilon_{xx} &= \frac{\delta u}{dx} \\ \varepsilon_{yy} &= \frac{\delta v}{dy} \\ \varepsilon_{xy} &= \frac{1}{2}\left(\frac{\delta u}{dy} + \frac{\delta v}{dx}\right) \\ \varepsilon_{yx} &= \frac{1}{2}\left(\frac{\delta u}{dy} + \frac{\delta v}{dx}\right) \end{aligned} \tag{3}$$

and the strain rate as

$$\dot{\varepsilon}_{ij} = \frac{\varepsilon_{ij}}{\delta t}. \tag{4}$$

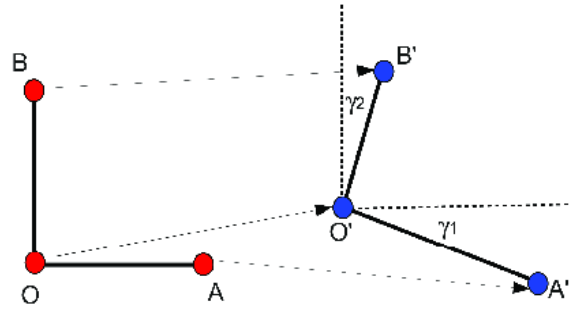

Figure 3. Schematic illustration related to the formulation of the strain tensor and calculation of the principal strains. The starting point is described by three points (e.g. buoy locations); indicated by the three red dots. After a time shift there has occurred some spatial displacement of the locations and in the orientation angles (γ_1, γ_2); new locations indicated by the blue dots.

As strain tensor is a (real) symmetric matrix, it can be represented as a set of orthogonal eigenvectors, directions along which there is no shear, only stretching or compression. The principal strains (ε_1,ε_2) are the eigenvalues of the strain tensor. The relative change in the lengths of the two sides by definition gives the strain, for the 1st diagonal component the equation becomes: $\varepsilon_{xx} = |OA - O'A'| / |OA|$. The shear strain is the angular distortion and is given by $\varepsilon_{xy} = (\gamma_1 + \gamma_2)/2$.

We used the virtual buoys to calculate the strain rates as function of the time. We calculated the average strain rate for each time step by first calculating the strain rates for every three-buoy combination of the virtual buoys and then by calculating the means of the individual strain rates. We used two approaches in the calculation. The first one was to exclude all the stationary buoys (the located in the fast ice area). The second was to use the stationary buoys as points O (O = O' in image 3, displacements only in locations of A and B).

The first approach gives the strains rates within the moving buoy system or the ice area where the buoys are located. As we can observe from the leftmost case of figure 1, the buoy movements are quite parallel. We computed the result in Figure 4a (for the Feb 25, 2011 case) from these movements. The strain rates remain almost at the same levels. No clear compression or extension can be observed. In the Figure 4b the same time series is computed by using the stationary buoys as points O. Now we can observe clear changes in the compression and extension. Between UTC 12:50 and UTC 13:32 a discharge of the ice compression occurred. This also roughly corresponds to the low ice drift velocity period visible in Fig. 2. After that there is again an increase in the compression. In the rightmost case of Figure 1, the tracks are not parallel to each other. Now we can observe a similar behavior in the results of both the approaches. In Figure 5a from the first one, and in Figure 5b from the second one. These figures also represent the Jan 20, 2013 case. Interesting is that the first approach better picks up the first compression case and the latter the second compression case.

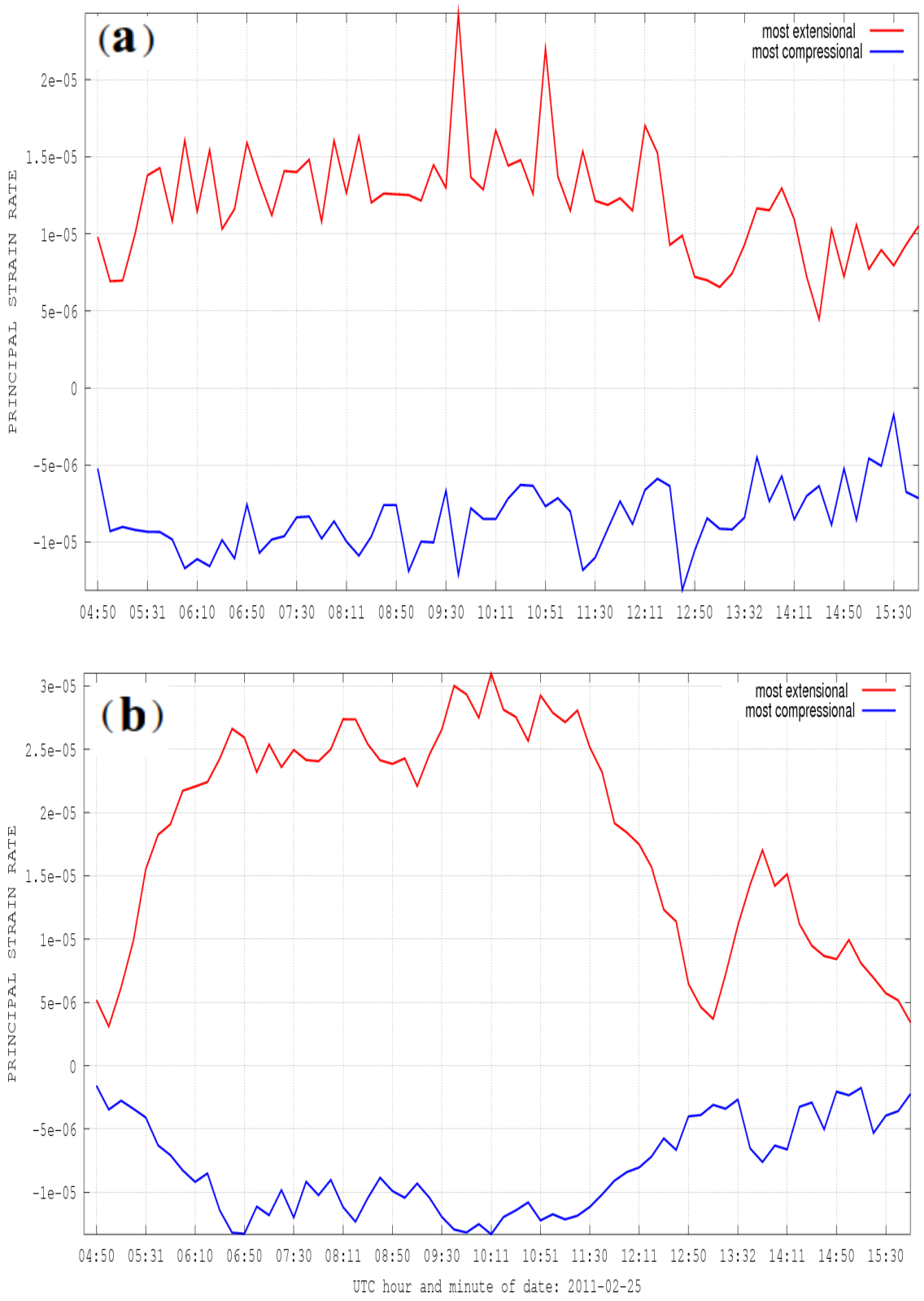

Figure 4. Example of mean principal strains computed on based virtual buoys for the Feb 25, 2011 case, ε_1 as red and ε_2 as blue. The time step is 10 min.

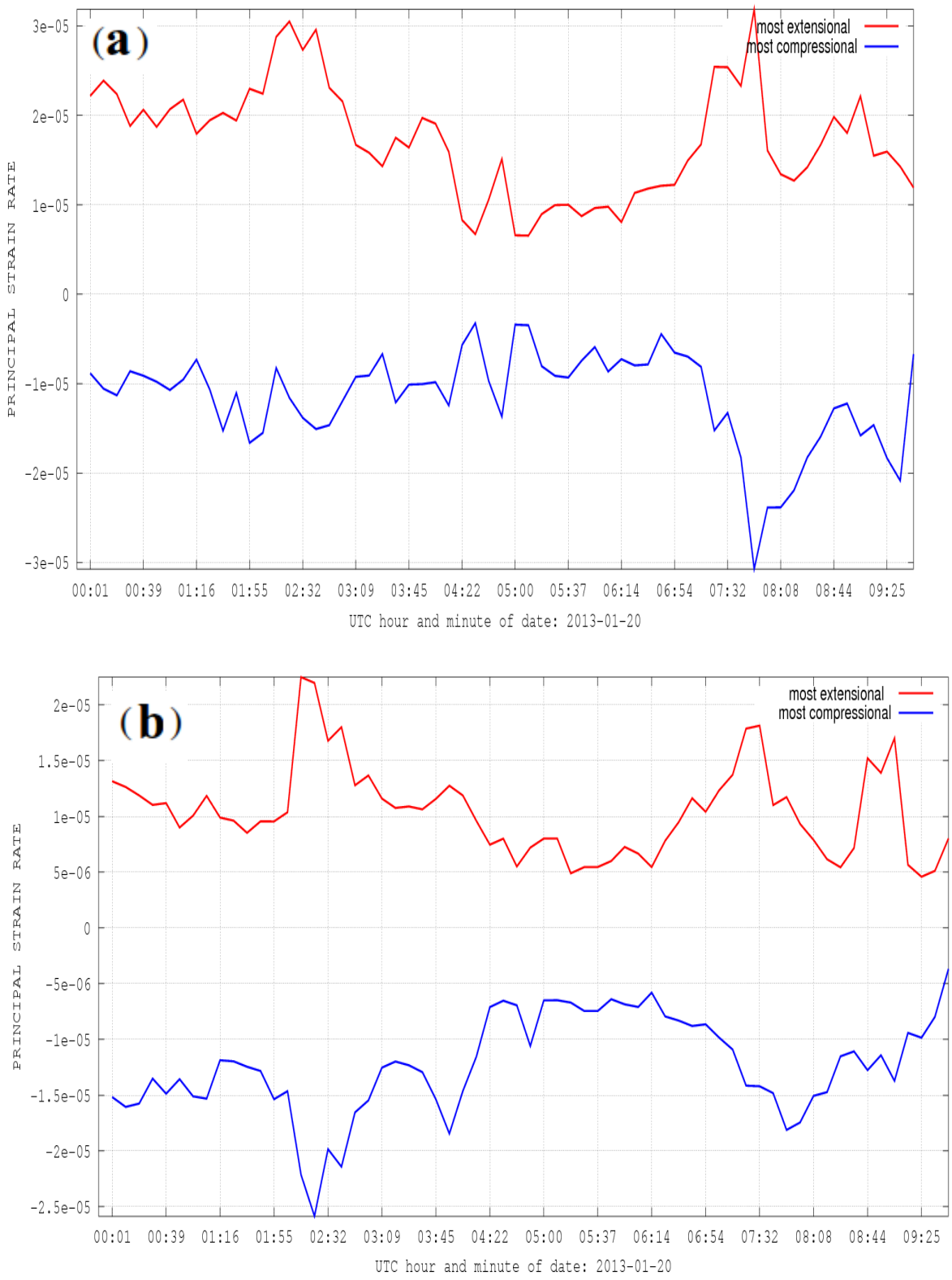

Figure 5. Example of mean principal strains computed based on virtual buoys for the Jan 20, 2013 case, ε_1 as red and ε_2 as blue. The time step is 10 min.

6. COMPARISON TO MODELLED ICE COMPRESSION

The ice compression is expressed as the internal stress of ice multiplied by an area of the model grid size. The grid size for the operational HELMI ice model is one nautical mile (1852 m x 1852 m). The ice compression forecasting is based on the viscous-plastic multi-category sea ice model (Haapala 2000, Haapala et al. 2005). This ice compression modelling is described in detail in (Eriksson et al., 2009). Here we only show figures describing the magnitude of the compressive force for the three Tankar test cases in Figures 6-8. The compression in the figures are scaled such that the maximum compression value appears as white and zero compression as black. For the Feb 25, 2011 case the maximum value was around 1600N, for the Feb 8, 2012 case around 800N, and for the Jan 20, 2013 case around 1500N. In the figures we can at least see that the compression forecasts near the coastal radar increase in the case of ice motion towards the fast ice and the coastal radar (2013) and decrease in the case of ice motion away from the fast ice (2011 and 2012).This indicates a correspondence between the virtual buoy observations and the modelled ice compression in areas where the drifting ice is either causing or releasing pressure against the fast ice field.

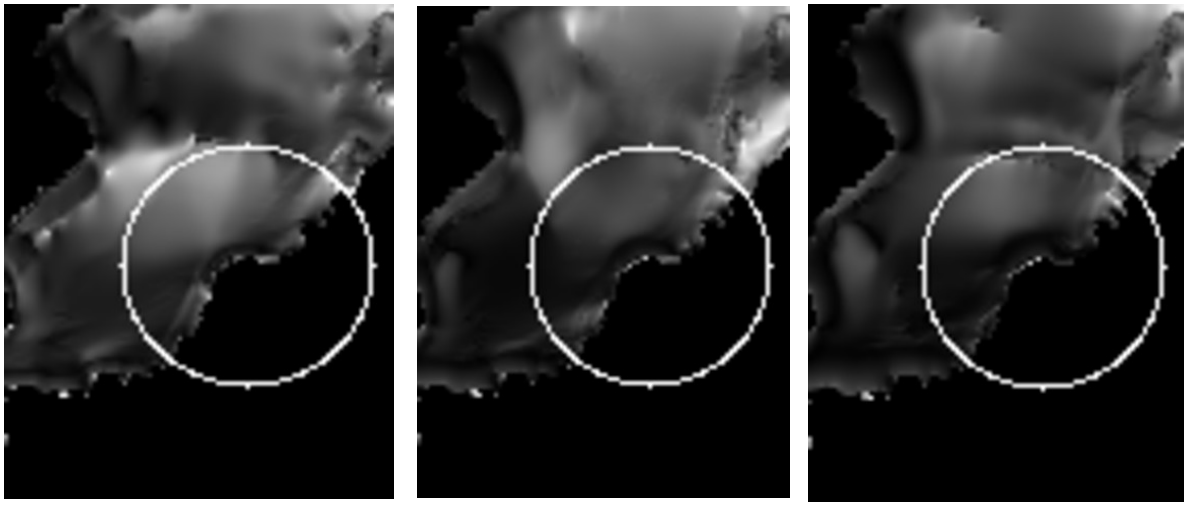

Figure 6. The compression forecast for Feb 25, 2011 test period, for the beginning of the period (left), in the middle of the period (middle), and at the end of the period (right). The coastal radar is located in the middle of the drawn white circle. Brighter tones indicate higher compression and darker tones lower compression. The compression near the fast ice zone is reduced during the period, as the ice is moving apart of the fast ice zone.

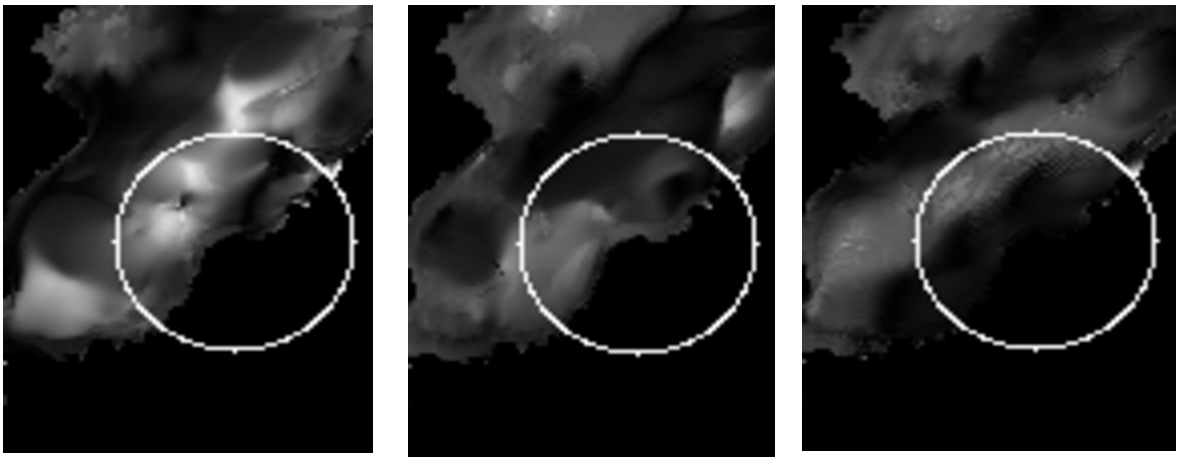

Figure 7. The compression forecast for Feb 8, 2012 test period, for the beginning of the period (left), in the middle of the period (middle), and at the end of the period (right). The coastal radar is located in the middle of the drawn white circle. Brighter tones indicate higher compression and darker tones lower compression. Similarly, as in Fig. 6, the compression near the fast ice zone is reduced during the period, as the ice is moving apart of the fast ice zone, and slightly growing in the mid parts of the gulf (in the direction of the ice drift).

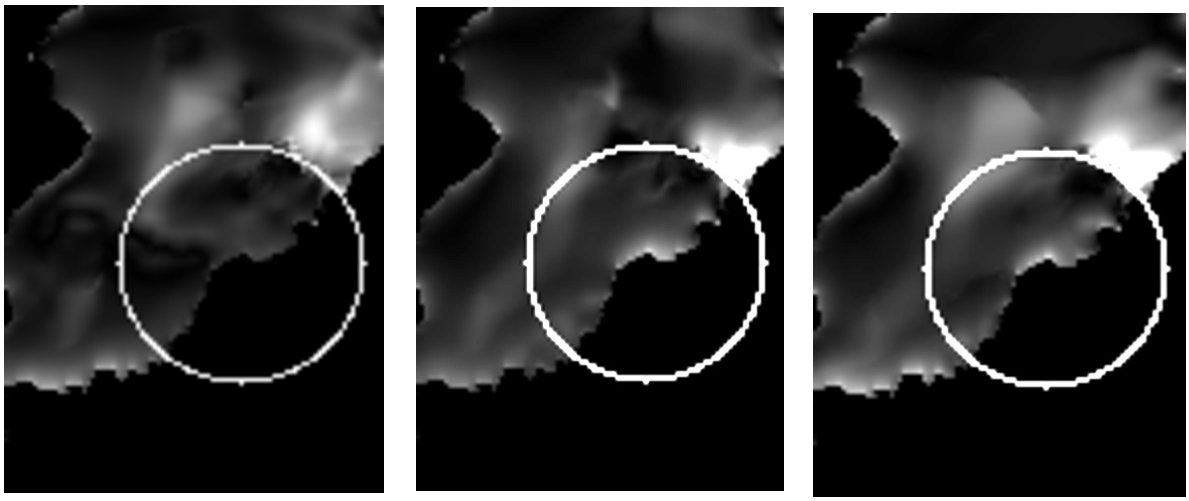

Figure 8. The compression forecast for Jan 20, 2013 test period, for the beginning of the period (left), in the middle of the period (middle), and at the end of the period (right). The coastal radar is located in the middle of the drawn white circle. Brighter tones indicate higher compression and darker tones lower compression. The compression near the fast ice zone is increased during the period, as the ice is moving towards of the fast ice zone.

7. CONCLUSION AND SUMMARY

We have shown that the virtual buoys can be used as substitutes to real buoys for computing quantities related to ice dynamics, such as strain rates. The time series of the strain rates agree with the visual interpretation of radar image sequences. We also made a qualitative visual

comparison between the ice compression between the ice compression forecasts for the cases studied, and noticed that at least in these cases the ice compression near the coastal radar decreases when the ice motion is away from the coastal radar, and increases in the opposite motion. We expect this methodology of generating and tracking virtual buoys to be used operationally in validation of ice models and in estimation of local coastal ice conditions in the future. In the operational mode, to enable continuous ice tracking, the algorithm should be able to generate new virtual buoys in the vicinity of the coastal radar after the number of virtual buoys has reduced in the course of time, due to the drifting of the virtual buoys too far away from the coastal radar for reliable tracking.

REFERENCES

Eriksson, P., Haapala J., Heiler I., Leisti H., Riska K., Vainio J., 2009, Ships in compressive ice, Description and Operative Forecasting of Compression in an Ice Field, Research report n. 59, Winter navigation research board (of Finnish and Swedish maritime administrations).

Haapala J., 2000, On the modelling of ice-thickness redistribution. J. Glaciol., 46(154), 427–437, doi:10.3189/172756500781833106.

Haapala J, Lonnroth N., and Stossel A., 2005, A numerical study of open water formation in sea ice. J. Geophys. Res., 110(C9), C09011, doi: 10.1029/2003JC002200.

Harris C., and M. Stephens, 1988, A Combined Corner and Edge Detector, Proc. of Alvey Vision Conference, Univ. of Manchester, pp. 147-151.

Karvonen J, 2012, Tracking the motion of recognizable sea-ice objects from coastal radar image sequences, Annals of Glaciology, v. 54, pp. 41-49.

Ojala, T., M. Pietikainen, D. Harwood, 1996. A Comparative Study of Texture Measures with Classification Based on Feature Distributions, Pattern Recognition, v. 29, pp. 51-59.